Boosting the catalytic performance of single-atom catalysts by tuning surface lattice expanding confinement

Fei Gao,[a,†,*] Annai Liu,[b,†] Wei Tan,[a,†] Bing Hu,[c] Ruihan Gong,[a] Xing Cheng,[d] Fudong Liu,[e] Ge Chen,[d] Lin Dong[a]

[a] *State Key Laboratory of Pollution Control and Resource Reuse, School of Environment; Jiangsu Key Laboratory of Vehicle Emissions Control, Center of Modern Analysis; Key Laboratory of Mesoscopic Chemistry of MOE, School of Chemistry and Chemical Engineering, Nanjing University, Nanjing 210023, China*

[b] *Institute of Engineering Technology, Sinopec Catalyst Co. Ltd., Sinopec Group, 13 Xingguang 5th Avenue, Beijing 101111, P. R. China*

[c] *Institute for Catalysis, Hokkaido University, Kita 21 Nishi 10, Kita-ku, Sapporo, Hokkaido 001-0021, Japan*

[d] *College of Environmental and Energy Engineering, Beijing University of Technology, Pingle yuan 100, Beijing 100124, P.R. China*

[e] *Department of Civil, Environmental, and Construction Engineering, Catalysis Cluster for Renewable Energy and Chemical Transformations (REACT), NanoScience Technology Center (NSTC), University of Central Florida, Orlando, FL 32816, United States*

[†] These authors contributed equally to this work.

Corresponding Authors: gaofei@nju.edu.cn (F. Gao)

Methods

Pretreatment of TiO_2. 10 g rutile TiO_2 powder was placed in a tube furnace and treated with different gas flows at a rate of 200 mL/min. At a ramp of 5 K/min, the powder was heated to 873 K and held at 873 K for 1 h. With the inlet gas containing 20% O_2/Ar, 7% H_2/Ar or pure H_2, TiO_2-Wt (BET surface area of 24 m^2/g), TiO_2-Gr (24 m^2/g) or TiO_2-Dg (23 m^2/g) was produced, respectively. Wt, Gr and Dg stand for the apparent color (white, gray and dark gray) of collected samples. (**Fig. S1**)

Synthesis of catalysts. After ultrasonically dispersed in 50 mL deionized water, 2 g pretreated TiO_2 powder was stirred for 1 h. A 50 mL solution containing 3.96 mg $Pt(NH_3)_4(NO_3)_2$ was then added dropwise. This suspension was then stirred for 3 h and dried with rotary evaporation. The product was further dried at 100 ℃ overnight, ground and calcined in a tube furnace in the presence of flowing 20% O_2 in Ar at a rate of 200 mL/min. The heating ramp was 2 K/min. The calcination was held at 573 K for 2 h, forming samples with 0.1 wt% Pt loadings, designated as Pt_1/TiO_2-Wt, Pt_1/TiO_2-Gr and Pt_1/TiO_2-Dg.

Characterization. The X-ray diffraction (XRD) patterns of these samples were tested on a Philips X'pert Pro diffractometer using Ni-filtered Cu Kα radiation (λ = 0.15 nm). The X-ray tube was operated at 40 kV and 40 mA. The N_2 adsorption at 77 K was applied for the test of BET surface areas of the TiO_2 samples on a Micrometrics ASAP 2020 adsorption apparatus. All samples were degassed at 573 K for 3 h before the test. Electron paramagnetic resonance (EPR) spectra were recorded at 110 K on a Bruker EMX-10/12 X-band spectrometer operating at a frequency of ν ≈ 9.48 GHz, and 100 kHz field modulation was used for the measurements. The aberration corrected high resolution scanning transmission electron microscopic (AC-HR-STEM) images were collected on a probe-corrected FEI Titan 80-300 electron microscope. The observations were performed in the high angle annular dark field (HAADF) mode, which allows Z-contrast imaging. The probe convergence angle was approximately 18 mrad and the inner detection angle on the HAADF detector was approximately 3 times higher than the probe convergence angle. The bright field (BF) HRTEM images were collected on a JEM-2100 transmission electron microscopy. To prepare the TEM samples, an appropriate amount of the sample powder was dispersed in ethanol and then dropped on a 3 mm TEM Cu grid. The X-ray absorption fine spectroscopy (XAFS) were measured at Beijing synchrotron radiation facility (BSRF, Beijing, China). The Pt-L_3 edge XAFS were collected on the 1W1B beamline of BSRF in

fluorescence mode with Pt foil and PtO_2 as references. The Ti-K edge XAFS were collected on the same beamline in transmission mode. The XAFS of Ti-L_3 and O-K edges were also collected on the 4B9B beamline of BSRF. The electron beam energy of the storage ring was 2.5 GeV with a stored current of 200 mA. The XAFS data were processed with REX2000 (Rigaku) and IFEFFIT analysis package.[1, 2] Raman Spectroscopic measurements were performed on a LabRAM Aramis laser Raman spectroscopy using a laser (532 nm) with the power of 5 mW. The UV-Vis diffuse reflectance spectra were obtained on a Shimadzu UV-2401 spectrometer with $BaSO_4$ as reference. *In situ* diffuse reflectance infrared Fourier transform spectroscopy (DRIFTS) was carried out on a Nicolet 5700 FT-IR spectrometer equipped with an MCT detector. The spectra were collected from 400 to 4000 cm^{-1} at a spectral resolution of 4 cm^{-1} for 32 scans. Before the test, ca. 20 mg sample was pressed and mounted in the cup of the reaction chamber and purged with 1% O_2/He at 473 K for 1 h. The *in situ* CO adsorption test was carried out in the same gaseous environment as the catalytic CO oxidation test at 373 K. The temperature-programmed oxidation of adsorbed CO (CO_{ad}-TPO) was performed with our previously reported method.[3] Typically, after the equilibrium adsorption of CO at room temperature, 1 % O_2/He was introduced with elevated temperature. The ramp rate of temperature is 10 K/min, with a spectrum collected every 5 K.

CO Oxidation Catalysis. The reaction was carried out in a fixed-bed reactor, where the data was collected by an online gas chromatograph equipped with two columns, a flame ionization detector (FID) and a thermal conductivity detector (TCD) used for analyzing the products. In a typical test, 50 mg sample, diluted with 450 mg SiC, was purged with 2% O_2/He with a rate of 30 mL/min at 473 K. The feed was 1% CO and 1% O_2 in He with a total rate of 25 mL/min, corresponding to a space velocity of 30,000 cm^3(STP)/(g·h). All CO conversions were kept below 10%.

The catalytic rate *v* was calculated by

$$v = \frac{\left(1 - \frac{[CO]_{out}}{[CO]_{in}}\right) \times 1.0\% \times 0.025\ L/min}{22.4\ L/mol \times \frac{m_{Pt}}{195\ g/mol} \times 60\ s/min}$$

Computational method. All density functional theory (DFT) calculations were performed using Vienna Ab initio Simulation Package (VASP).[4, 5] The generalized gradient approximation (GGA) with the Perdew-Burke-Ernzerhof (PBE) functional was applied with the cutoff of 400 eV.[6] A four-layer rutile TiO_2(101) surface was constructed with half of the layers at the bottom fixed in all the

calculations. A geometry optimization was considered with the convergency of force wo be smaller than 0.05 eV/Å. The transition states were located using the constrained optimization.[7] A Monkhorst-Pack k-point of 2×2×1 was applied in all the calculations. Standard free energy corrections were performed by the equation: $\Delta G = \Delta E_{DFT} + \Delta E_{ZPE} + \Delta E_U - T\Delta S$, where ΔE_{DFT} is the DFT electronic energy difference of each step, ΔE_{ZPE}, ΔE_U and ΔS are the correction of zero-point energy, inner energy and entropy, respectively.[8, 9] The free energy corrections for gas phase molecules were performed by Gaussian calculations, and the free energy corrections for adsorbates were obtained by the vibrational frequency calculations through VASP. In addition, the effect from the Hubbard U corrections were considered beyond the accuracy of DFT calculations of GGA, where U values (employed as U - J) of 4.2 for Ti.[10]

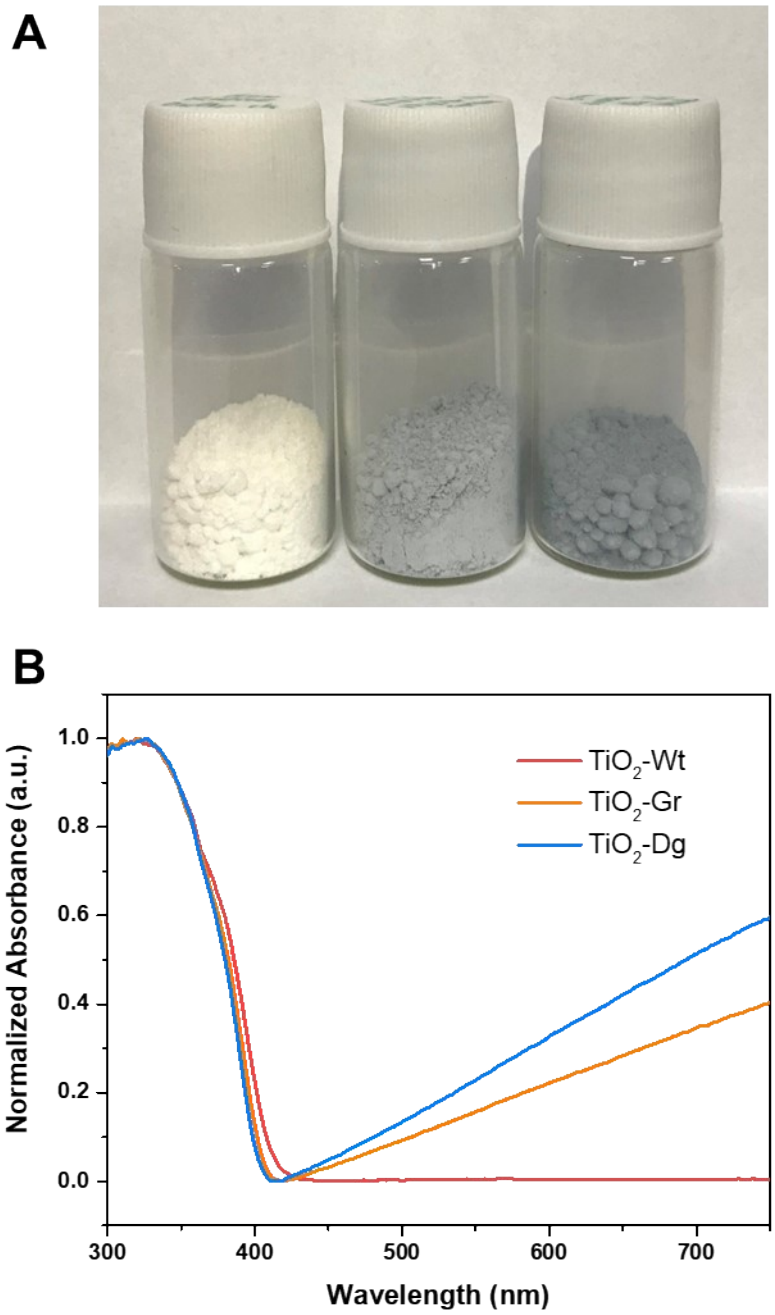

Fig. S1 (A) The digital photograph of TiO_2-Wt, TiO_2-Gr, and TiO_2-Dg. (B) The UV-vis spectra of TiO_2 samples. Compared to TiO_2-Wt, TiO_2-Gr and TiO_2-Dg show strong absorption in the visible light region of UV-vis spectra.

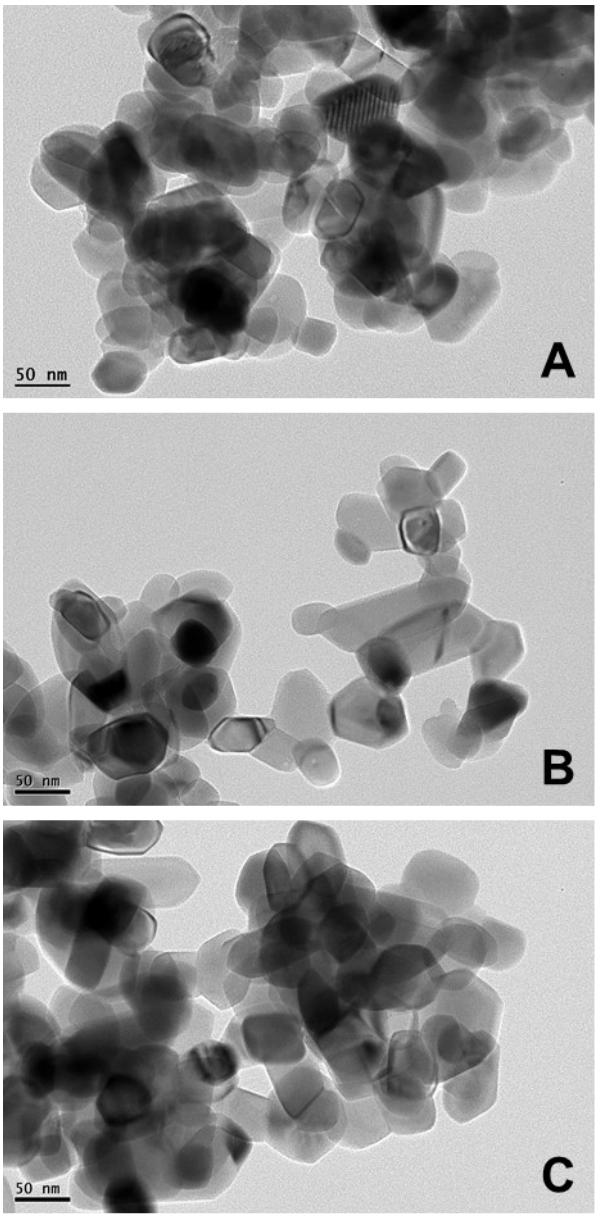

Fig. S2 The BF-TEM images of (A) TiO_2-Wt, (B) TiO_2-Gr, and (C) TiO_2-Dg. All 3 samples contain TiO_2 crystals with sizes of *ca.* 50 nm.

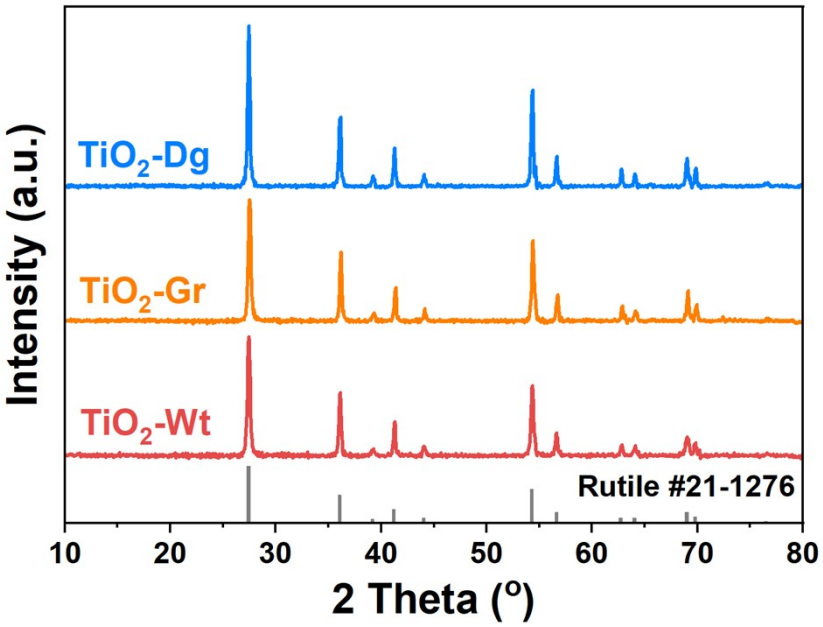

Fig. S3 The XRD patterns of TiO_2 samples. In all 3 samples, TiO_2 crystals show typical rutile structures. (JCPDS #21-1276)

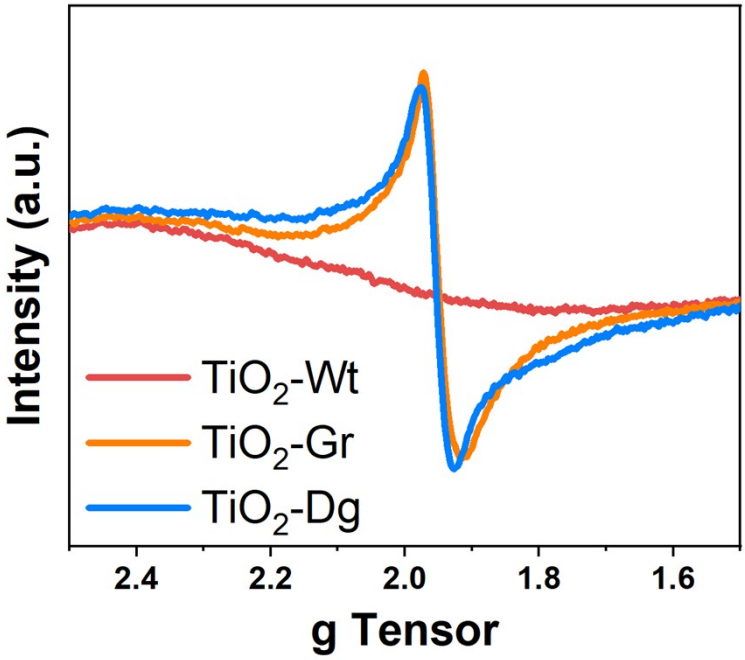

Fig. S4 The low-temperature EPR of different TiO_2 samples.

Because of the unpaired electron in the [Ar]$3d^1$ configuration, the Ti^{3+} species in the rutile nanocrystals can be detected by low-temperature electron paramagnetic resonance (EPR) spectroscopy.[11, 12] The EPR signals at g = 1.95 indicated that Ti^{3+} species are present in TiO_2-Gr and TiO_2-Dg samples, while not in TiO_2-Wt.

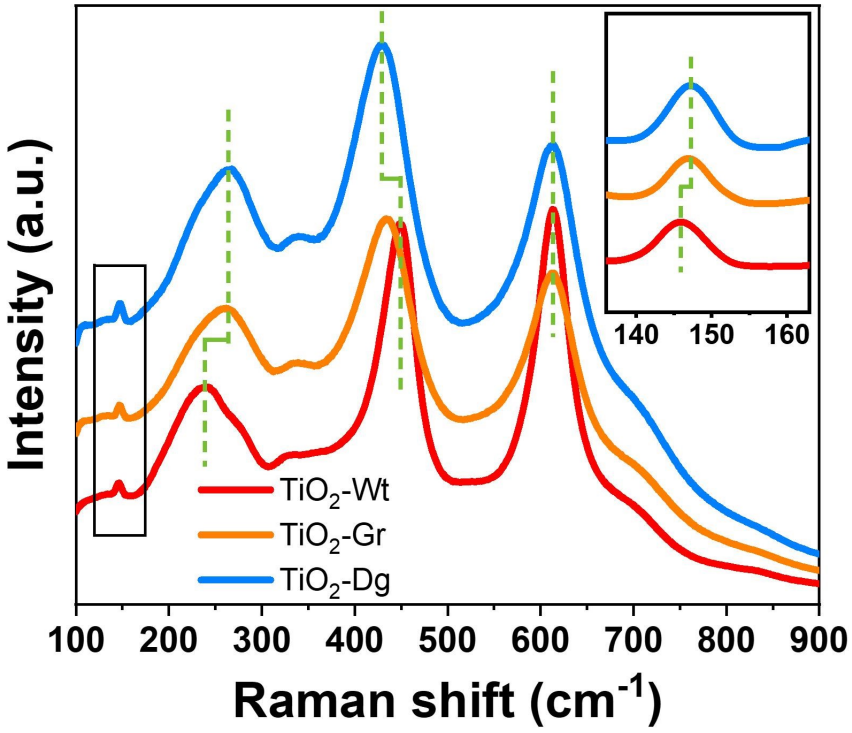

Fig. S5 The Raman spectra of TiO_2 samples, inset amplifying the blue square in this figure.

Raman spectra of these samples were collected to understand the geometric structural change in the TiO_2 surface. As shown in **Fig. S5**, in the case of TiO_2-Wt, its Raman spectrum indicates a typical rutile structure, presenting the peaks at ca. 146, 450 and 612 cm^{-1} ascribed to the vibration modes of B_{1g}, E_g and A_{1g}, respectively. The peak at ca. 240 cm^{-1} is relevant to the second order Raman scattering.[13, 14] Compared to TiO_2-Wt, shifts of Raman bands at 146, 240, and 450 cm^{-1} can be observed on TiO_2-Gr and TiO_2-Dg samples, indicating the change of surface structures of the H_2-treated TiO_2. For instance, the redshift of peaks corresponding to the E_g mode (450 cm^{-1}) was related to the nonstoichiometric decrease of O/Ti ratio, which suggests the reduction of surface Ti^{4+} to Ti^{3+} and the formation of oxygen vacancies.[15] Moreover, more significant shifts in the Raman spectrum were observed on TiO_2-Dg than on TiO_2-Gr, suggesting a higher degree of surface structural changes after a deep reduction treatment with pure hydrogen.

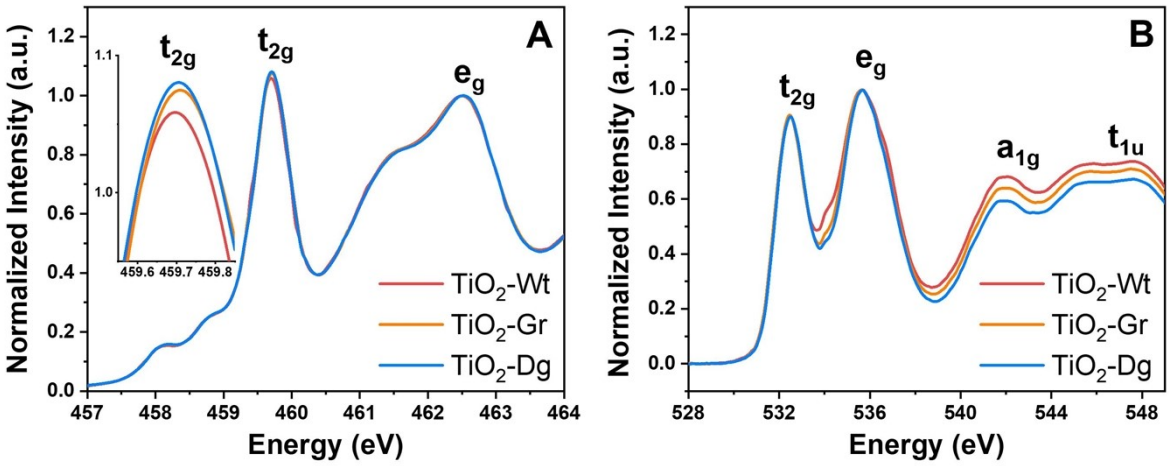

Fig. S6 (A) Ti-L_3 and (B) O-Kedge XANES of TiO_2-Wt, TiO_2-Gr, and TiO_2-Dg.

X-ray absorption fine spectroscopy (XAFS) of Ti-L_3 edge and O-K edge to study the density of state (DOS) of unoccupied orbitals in TiO_2 crystals. As can be seen in **Fig. S6**, the XANES of Ti-L_3 edge and O-K edge correspond to the electron transfers from Ti-2p→Ti-3d and O-1s→O-2p, respectively.[16] There are 2 peaks in the e_g normalized XANES of Ti-L_3 edge (ca. 460 eV and ca. 463 eV) assigned to the t_{2g} and e_g states (**Fig. S6A**), respectively. The slightly increased t_{2g} intensities of reduced TiO_2 samples suggest the increased ratios of unoccupied Ti-3dπ states in t_{2g} bonds. For e_g normalized O-K edge XANES depicted in **Fig. S6B**, as the degree of surface reduction increased, the narrowed e_g peak and decreased a_{1g} and t_{1u} intensities indicate the change of local symmetry and reduced long-range order.[17] Furthermore, it should be noted that although the Ti-K XAFS gives mainly the sample's structural information in bulk phase, the higher Debye-Waller factors for the fitting results of the reduced TiO_2 samples indicate the increase of the degree of surface disordering after the reduction treatments at high temperature (**Table S1**), which further proves the surface structural changes in the reduced TiO_2 concluded from TEM images and Raman spectra (See **Fig. S7-S10** and **Table S1**).

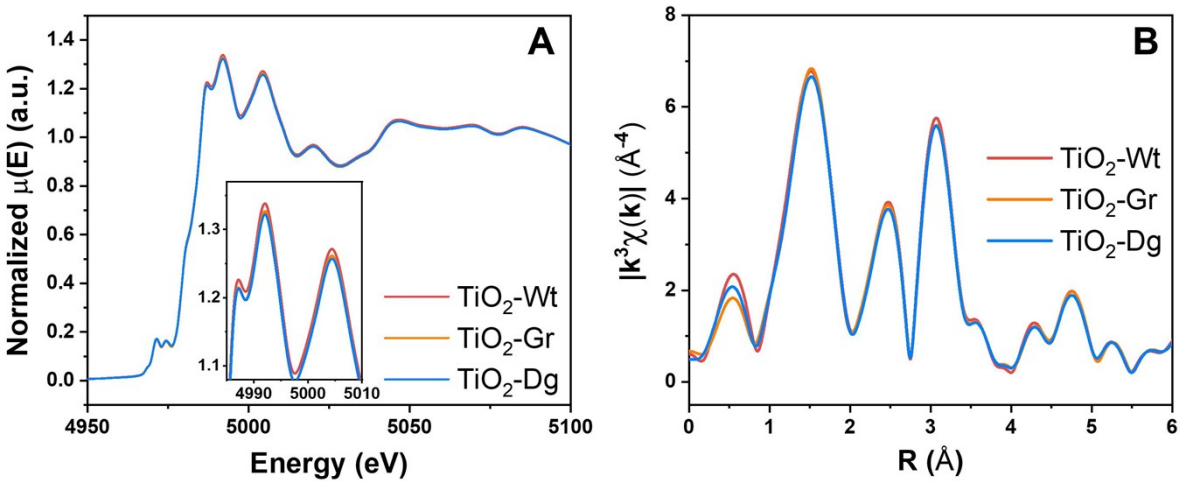

Fig. S7 The (A) XANES and (B) EXAFS of TiO_2 samples with insets showing the white line.

To study the geometric and electronic structural differences among these TiO_2 samples, we have also performed the Ti-K edge XAFS for all three samples. As can be seen in **Fig. S7A**, the slightly lower white line in the XANES of the reduced TiO_2 samples compared with the pristine TiO_2-Wt sample also proves the partial reduction of the TiO_2 surface, which is in line with the results of EPR spectra. For the Ti-K edge EXAFS (see **Fig. S7B**, **Fig. S8–S10**, and **Table S1**), a series of very similar spectra and fitting results are obtained for the three TiO_2 samples, regardless of the treatments. Such results are reasonable because EXAFS is a technique that measures the sample's structural information in bulk phase. The EXAFS results are also consistent with the structural information inferred from TEM and XRD, indicating the perseverance of bulk properties of the rutile nanocrystals during high-temperature reduction treatment.

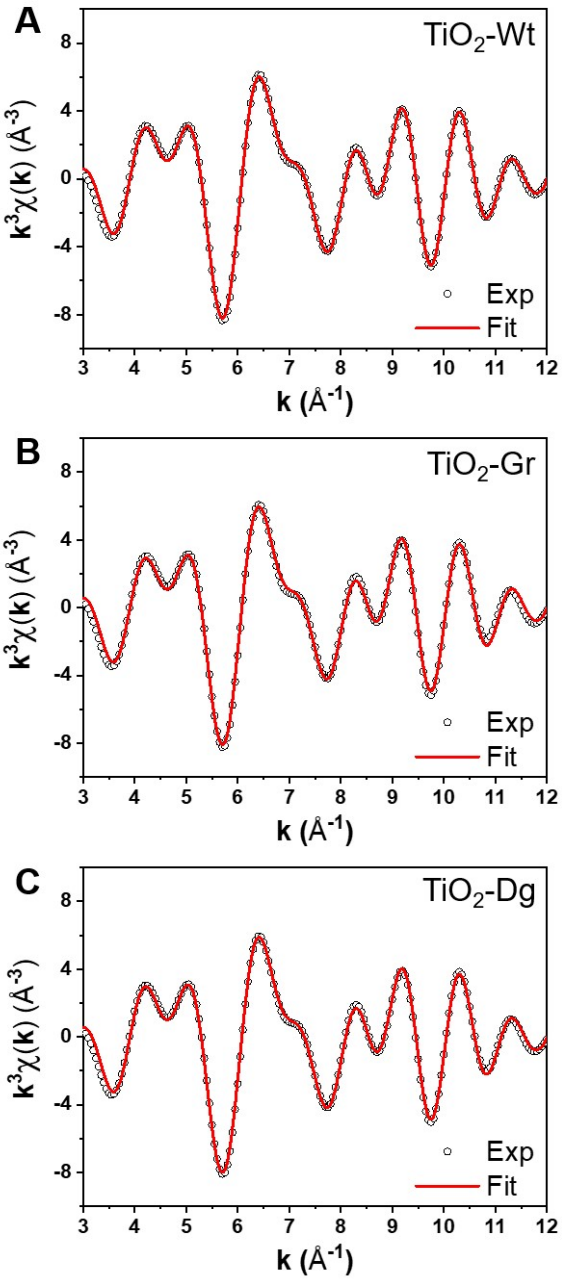

Fig. S8 The k^3 weighted Ti-K EXAFS function of the corresponding region of fitting area (experiment results, open circle) and fitting results (red line) of (A) TiO_2-Wt, (B) TiO_2-Gr, and (C) TiO_2-Dg.

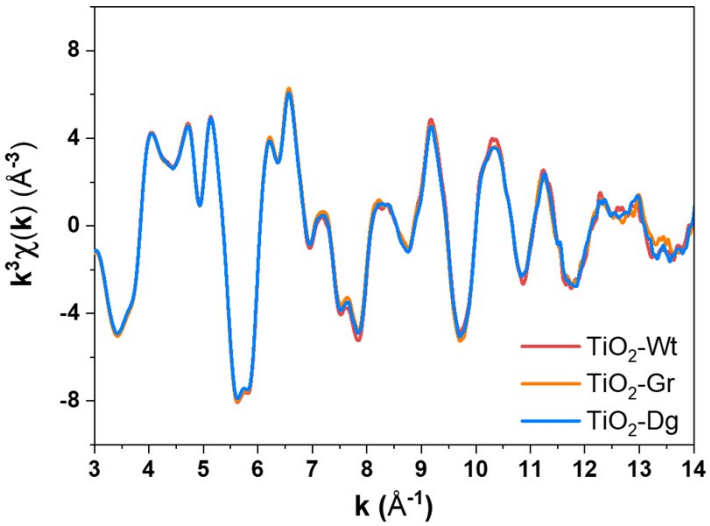

Fig. S9 The k^3 weighted Ti-K EXAFS function of TiO_2-Wt, TiO_2-Gr, and TiO_2-Dg.

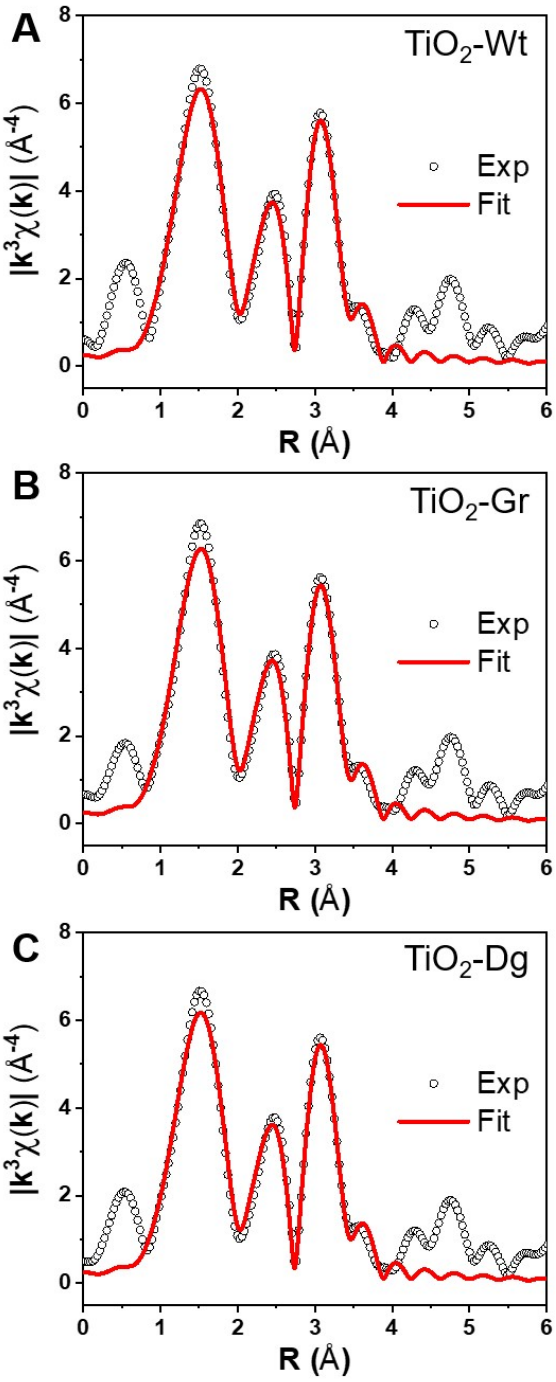

Fig. S10 The Ti-K edge EXAFS data (open circle) and the corresponding fitted curves (solid red line) in R space for (A) TiO_2-Wt, (B) TiO_2-Gr, and (C) TiO_2-Dg.

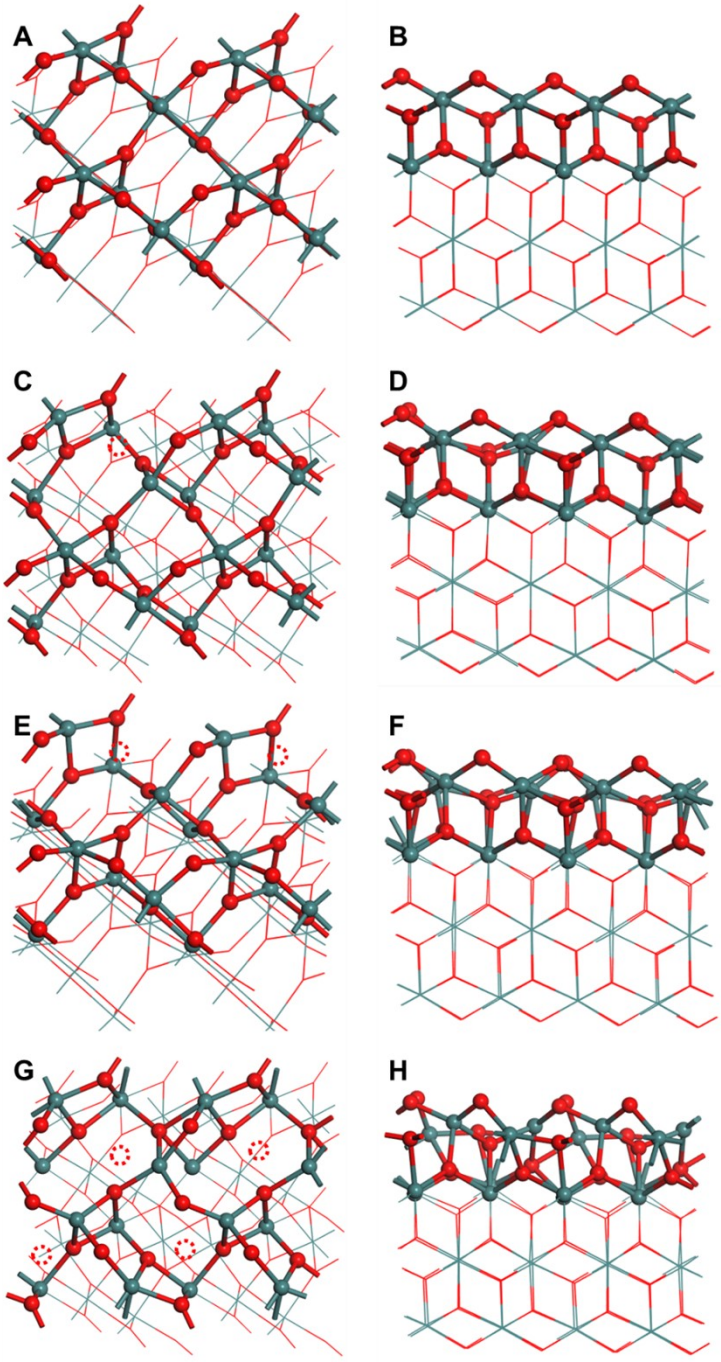

Fig. S11 Top-views (left) and side-views (right) of simulated TiO_2 structures. (A, B) The perfect TiO_2 structures. (C-H) The reduced TiO_2 structures with 1 (C, D), 2 (E, F), and 4 (G, H) oxygen atoms removed. The removed oxygen atoms were signified by red dotted circles. Green and red balls indicate Ti and O atoms, respectively.

We have examined the structural change of rutile TiO_2 through the reduction by removing some oxygen atoms of rutile (101) surface.[12] As shown in **Fig. S11**, the reduction progress, compromising the close-packed surface lattice structure, leads to the distortion of Ti-O bonding on the TiO_2 surfaces, which decreases the surface periodicity and creates expansion in the surface lattice.

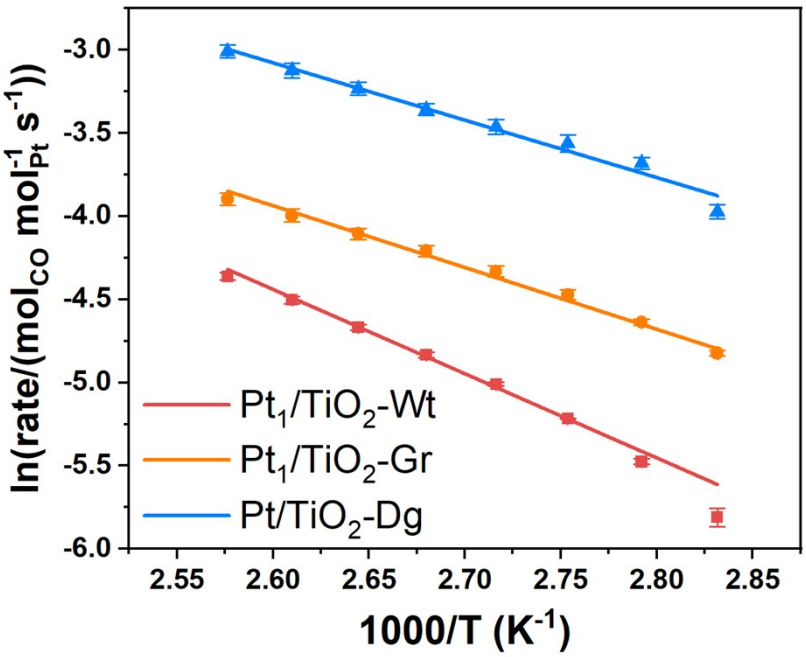

Fig. S12 The Arrhenius plot of Pt_1/TiO_2 samples for CO oxidation.

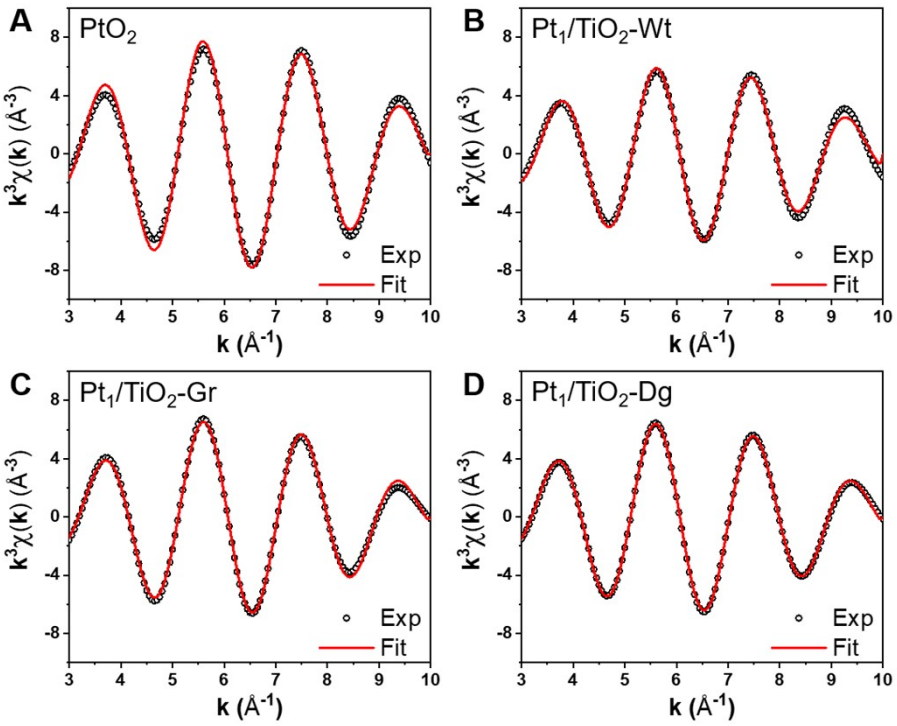

Fig. S13 The k^3 weighted Pt-L_3 EXAFS function of the corresponding region of fitting area (experiment results, open circle) and fitting results (red line) of (A) PtO_2, (B) Pt_1/TiO_2-Wt, (C) Pt_1/TiO_2-Gr and (D) Pt_1/TiO_2-Dg.

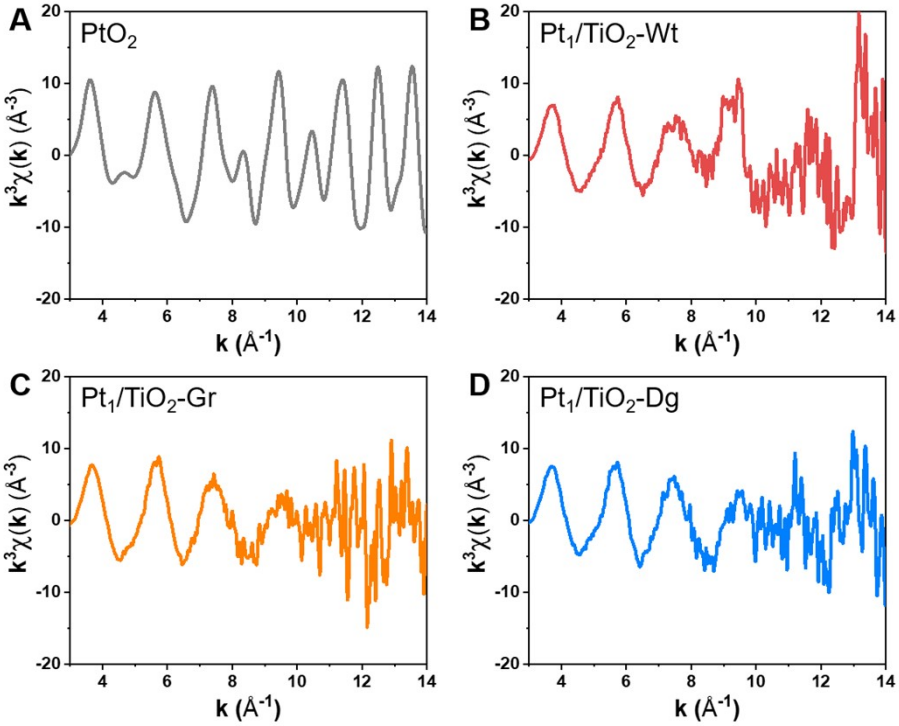

Fig. S14 The k^3 weighted Pt-L_3 EXAFS function of (A) PtO_2, (B) Pt_1/TiO_2-Wt, (C) Pt_1/TiO_2-Gr and (D) Pt_1/TiO_2-Dg.

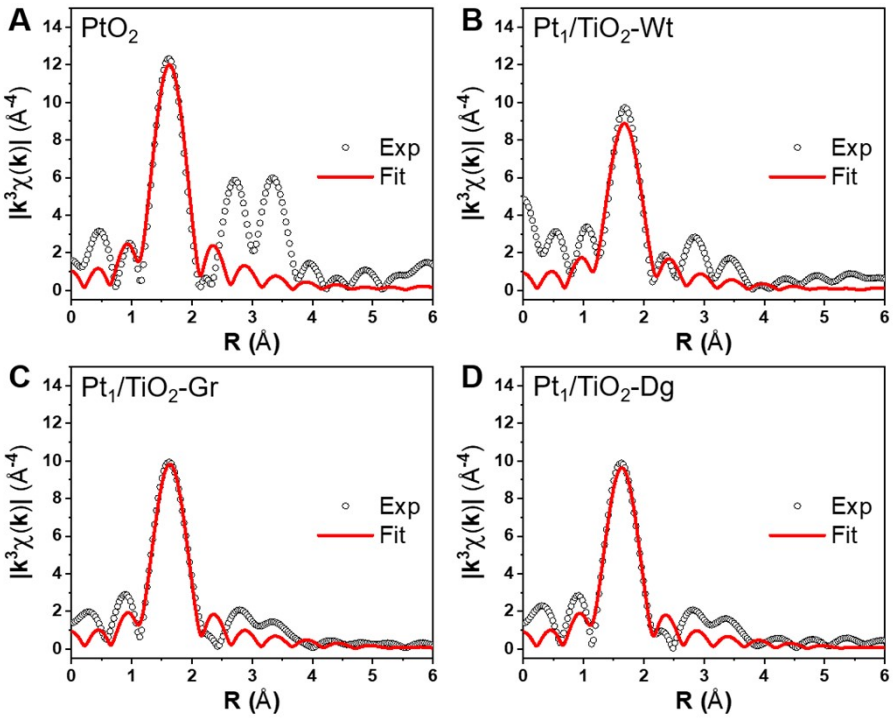

Fig. S15 The Pt L_3-edge EXAFS data (open circle) and the corresponding fitted curves (solid red line) in R space for (A) PtO_2, (B) Pt_1/TiO_2-Wt, (C) Pt_1/TiO_2-Gr and (D) Pt_1/TiO_2-Dg.

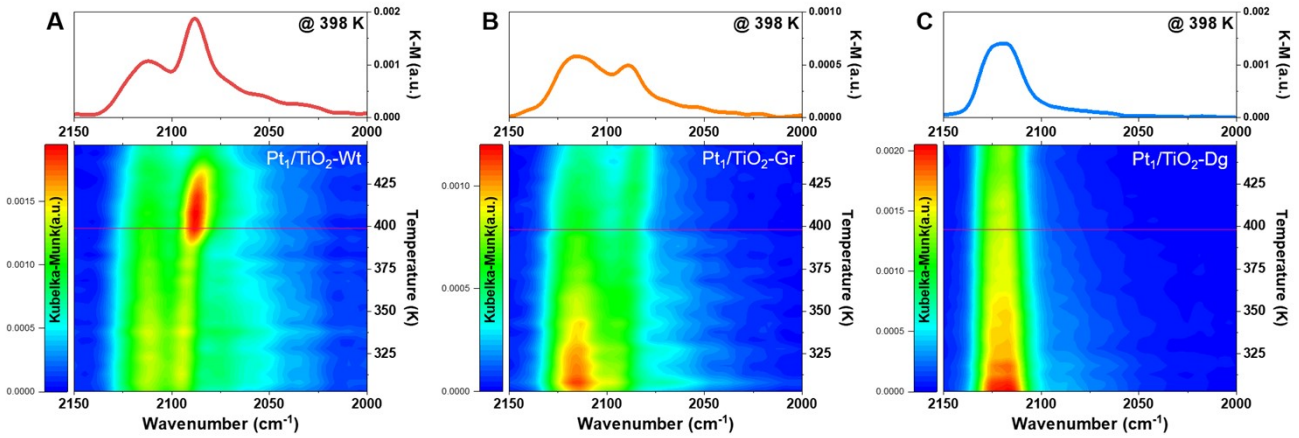

Fig. S16 The line profiles (up) at 398 K from the CO_{ad}-TPO profiles (down) of (A) TiO_2-Wt, (B) TiO_2-Gr, and (C) TiO_2-Dg.

To illustrate the evolution of Pt atoms at elevated temperature, we tested the TPO of the adsorbed CO. Typically, after equilibrium adsorption of CO at room temperature, 1% O_2/He was introduced to the Pt catalysts as the temperature was elevated. As shown in **Fig. S16A**, the band at ca. 2120 cm^{-1}, corresponding to the linear adsorption of CO on cationic Pt single atoms supported on TiO_2-Wt, shifted to lower wavenumbers. At low temperatures (<400 K), a very mild decrease of intensity is observed, indicating the *in situ* charge transfer between Pt single atoms and adsorbed CO molecules rather than the oxidation of the CO molecules to CO_2 on the Pt_1/TiO_2-Wt sample. This explains the low activity of catalytic CO oxidation of Pt_1/TiO_2-Wt. The band of adsorbed CO on Pt_1/TiO_2-Gr also shifted as temperature was increased, but not as significant as that of Pt_1/TiO_2-Wt (**Fig. S16B**), indicating the lower reduction tendency of Pt single atoms on the mildly reduced TiO_2 supports. Interestingly, as shown in **Fig. S16C**, the band center associated with CO adsorbed on Pt_1/TiO_2-Dg remained nearly unchanged during the TPO test, showing that the deeply reduced TiO_2 could stabilize Pt single atoms with high electron deficiency. In other words, by varying the surface properties of supporting materials (TiO_2 in this case), the structural and electronic properties of supported Pt single atoms could be finely tuned, which might give rise to better activities of these Pt atoms.

It is also noteworthy that, after reaction at higher temperatures, shoulder bands at *ca.* 2090 cm^{-1} are observed with Pt_1/TiO_2-Wt and Pt_1/TiO_2-Gr samples (**Fig. S16**), suggesting that part of the Pt single atoms agglomerated into nanoparticles at elevated temperature, which should be caused by the reduction of positively charged Pt atoms by CO.[18] In other words, the stabilization of isolated Pt

atoms with high electron deficiency by reduced TiO_2 surfaces not only promotes their catalytic performance for CO oxidation, but also prevents these atoms from agglomeration.

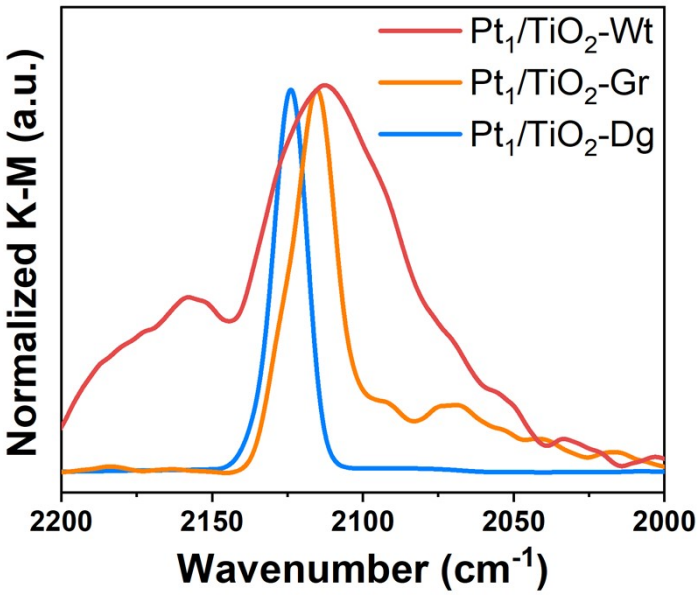

Fig. S17 *In situ* DRIFTS of CO adsorption (298 K) on used samples after CO oxidation test. The feeding gas contained 1% CO (He Balance).

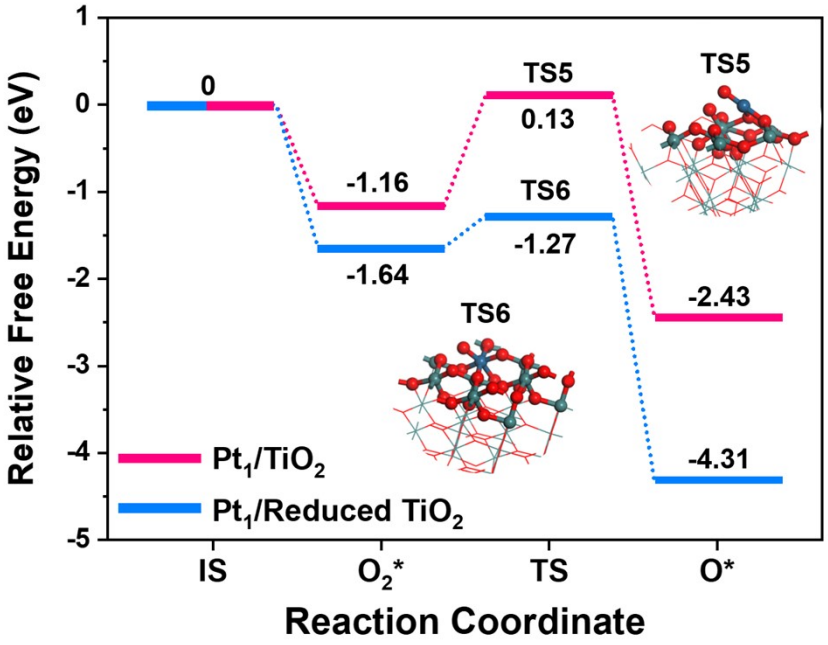

Fig. S18 The energy diagram of O_2 activation on Pt_1/perfect TiO_2 (pink) and Pt_1/reduced TiO_2 (blue) at 373 K. Both pathways are corrected to free energy. Blue, green, red balls indicate Pt, Ti, O atoms, respectively.

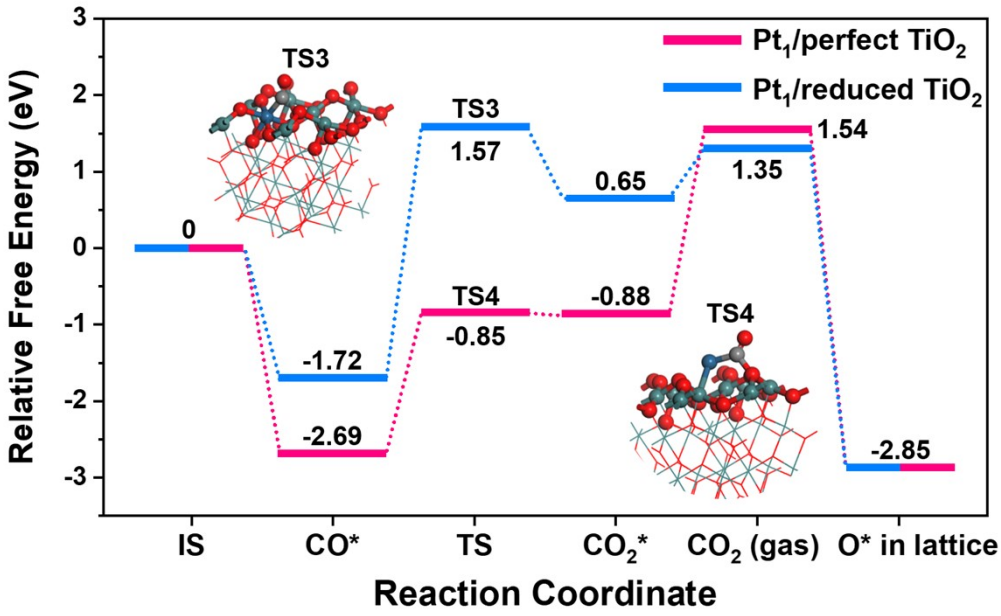

Fig. S19 The energy diagram of CO oxidation on Pt_1/perfect TiO_2 (pink) and Pt_1/reduced TiO_2 (blue) at 373 K via Mars-van Krevelen mechanism. All pathways are corrected to free energy. Blue, green, gray, red balls indicate Pt, Ti, C, O atoms, respectively.

As shown in **Fig. 4**, **Fig. S19** and **Table S3**, the energy barrier for CO oxidation with model S1 is lower than the L-H mechanism, yet still higher than that of S2 under the L-H mechanism. Nevertheless, the subsequent reaction of adsorbed CO and lattice oxygen would compromise the stability of the lattice expanded TiO_2 surface structure, making the MvK mechanism for S2 not favorable.

Table S1 Ti K-edge EXAFS fitting results (σ^2: Debye-Waller factor; *CN*: coordination number; *R*: distance; $\triangle E_0$: inner potential correction; k-range: 3.0-12.0 $Å^{-1}$ R-range: 0.8-3.8 Å) of TiO_2 samples.

Samples	Shells	*CN***	*R* (Å)	σ^2 (10^{-2} Å^2)	$\triangle E_0$ (eV)	s_0^2**	*R* factor (%)
	Ti-O	6	1.95	0.694			
TiO_2-Wt*	**Ti-Ti_1**	2	2.96	0.578	0	0.7	--
	Ti-Ti_2	8	3.57	0.859			
	Ti-O	6	1.94 ± 0.01	0.700 ± 0.051			
TiO_2-Gr	**Ti-Ti_1**	2	2.95 ± 0.01	0.604 ± 0.070	-1.0 ± 0.7	0.7	0.5
	Ti-Ti_2	8	3.56 ± 0.01	0.880 ± 0.041			
	Ti-O	6	1.94 ± 0.01	0.716 ± 0.044			
TiO_2-Dg	**Ti-Ti_1**	2	2.95 ± 0.01	0.626 ± 0.062	-1.0 ± 0.6	0.7	0.4
	Ti-Ti_2	8	3.56 ± 0.01	0.882± 0.036			

*TiO_2-Wt was chosen as the standard for the fitting of Ti-K edge of other samples.

**These values were fixed during the fitting procedures.

Table S2 Pt L_3-edge EXAFS fitting results (σ^2: Debye-Waller factor; *CN*: coordination number; *R*: distance; $\triangle E_0$: inner potential correction; k-range: 3.0-10.0 $Å^{-1}$ R-range: 1.2-2.2 Å) of Pt_1/TiO_2 samples.

Samples	*CN of Pt-O Shell*	*R* (Å)	σ^2 (10^{-2} Å)	$\triangle E_0$ (eV)
PtO_2	6*	2.02 ± 0.01	0.29 ± 0.19	4.7 ± 2.1
Pt_1/TiO_2-Wt	3.9 ± 0.6	2.05 ± 0.01	0.29 ± 0.25	2.0 ± 1.9
Pt_1/TiO_2-Gr	5.2 ± 0.5	2.02 ± 0.01	0.39 ± 0.11	-1.5 ± 1.1
Pt_1/TiO_2-Dg	4.6 ± 0.6	2.02 ± 0.01	0.23 ± 0.13	-1.5 ± 1.3

*These values were fixed during the fitting procedures.

Table S3 Elementary reaction energies of CO oxidation at on Pt_1/perfect TiO_2 and Pt_1/reduced TiO_2 at 373 K via Langmuir-Hinshelwood mechanism and Mars-van Krevelen mechanism.

Mechanism	Elementary reactions	Pt_1/perfect TiO_2		Pt_1/reduced TiO_2	
		Activation barrier (eV)	Reaction energy (eV)	Activation barrier (eV)	Reaction energy (eV)
L-H mechanism	CO + * → CO*		-2.69		-1.72
	CO* + O* → CO_2* + *	2.97	0.78	0.85	0.39
	CO_2* → CO_2 + *		0.28		0.63
	O_2 + *→ O_2*		-1.16		-1.64
	O_2* + * → 2O*	1.29	-1.27	0.37	-2.67
MvK mechanism	CO + * → CO*		-2.69		-1.72
	CO* + O* → CO_2* + *	1.84	1.81	3.29	2.37
	CO_2* → CO_2 + *		2.42		0.70
	O_2 + *→ O_2*		-3.50		-2.65
	O_2* + * → 2O*	0.01	-5.27	0.03	-5.75

References

1. T. Taguchi, T. Ozawa and H. Yashiro, *Phys. Scr.*, 2005, 205.
2. B. Ravel and M. Newville, *J. Synchrot. Radiat.*, 2005, **12**, 537-541.
3. A. Liu, X. Liu, L. Liu, Y. Pu, K. Guo, W. Tan, S. Gao, Y. Luo, S. Yu, R. Si, B. Shan, F. Gao and L. Dong, *ACS Catal.*, 2019, **9**, 7759-7768.
4. G. Kresse and J. Furthmüller, *Comput. Mater. Sci.*, 1996, **6**, 15-50.
5. G. Kresse and J. Hafner, *Phys. Rev. B*, 1994, **49**, 14251-14269.
6. J. P. Perdew, K. Burke and M. Ernzerhof, *Phys. Rev. Lett.*, 1996, **77**, 3865-3868.
7. H. F. Wang and Z. P. Liu, *J. Am. Chem. Soc.*, 2008, **130**, 10996-11004.
8. X. M. Cao, R. Burch, C. Hardacre and P. Hu, *Catal. Today*, 2011, **165**, 71-79.
9. Z. Wang, X. Liu, D. W. Rooney and P. Hu, *Surf. Sci.*, 2015, **640**, 181-189.
10. S. Chrétien and H. Metiu, *J. Phys. Chem. C*, 2011, **115**, 4696-4705.
11. A. Naldoni, M. Altomare, G. Zoppellaro, N. Liu, Š. Kment, R. Zbořil and P. Schmuki, *ACS Catal.*, 2019, **9**, 345-364.
12. A. T. Brant, E. M. Golden, N. C. Giles, S. Yang, M. A. R. Sarker, S. Watauchi, M. Nagao, I. Tanaka, D. A. Tryk, A. Manivannan and L. E. Halliburton, *Phys. Rev. B*, 2014, **89**, 115206.
13. O. Frank, M. Zukalova, B. Laskova, J. Kürti, J. Koltai and L. Kavan, *Phys. Chem. Chem. Phys.*, 2012, **14**, 14567-14572.
14. V. Swamy, B. C. Muddle and Q. Dai, *Appl. Phys. Lett.*, 2006, **89**, 163118.
15. J. C. Parker and R. W. Siegel, *Appl. Phys. Lett.*, 1990, **57**, 943-945.
16. G. Xiang, Y. Tang, Z. Liu, W. Zhu, H. Liu, J. Wang, G. Zhong, J. Li and X. Wang, *Nano Lett.*, 2018, **18**, 7809-7815.
17. V. S. Lusvardi, M. A. Barteau, J. G. Chen, J. Eng, B. Frühberger and A. Teplyakov, *Surf. Sci.*, 1998, **397**, 237-250.
18. L. Liu, D. M. Meira, R. Arenal, P. Concepcion, A. V. Puga and A. Corma, *ACS Catal.*, 2019, **9**, 10626-10639.